

Ship-Based Observations of the Diurnal Cycle of Southeast Pacific Marine Stratocumulus Clouds and Precipitation

CASEY D. BURLEYSON

North Carolina State University, Raleigh, North Carolina

SIMON P. DE SZOEKE

Oregon State University, Corvallis, Oregon

SANDRA E. YUTER AND MATT WILBANKS

North Carolina State University, Raleigh, North Carolina

W. ALAN BREWER

NOAA/Earth System Research Laboratory, Boulder, Colorado

(Manuscript received 27 December 2012, in final form 11 July 2013)

ABSTRACT

The diurnal cycle of marine stratocumulus in cloud-topped boundary layers is examined using ship-based meteorological data obtained during the 2008 Variability of American Monsoon Systems (VAMOS) Ocean–Cloud–Atmosphere–Land Study Regional Experiment (VOCALS-REx). The high temporal and spatial continuity of the ship data, as well as the 31-day sample size, allows the diurnal transition in degree of coupling of the stratocumulus-topped boundary layer to be resolved. The amplitude of diurnal variation was comparable to the magnitude of longitudinal differences between regions east and west of 80°W for most of the cloud, surface, and precipitation variables examined. The diurnal cycle of precipitation is examined in terms of areal coverage, number of drizzle cells, and estimated rain rate. East of 80°W, the drizzle cell frequency and drizzle area peaks just prior to sunrise. West of 80°W, total drizzle area peaks at 0300 local solar time (LST), 2–3 h before sunrise. Peak drizzle cell frequency is 3 times higher west of 80°W compared to east of 80°W. The waning of drizzle several hours prior to the ramp up of shortwave fluxes may be related to the higher peak drizzle frequencies in the west. The ensemble effect of localized subcloud evaporation of precipitation may make drizzle a self-limiting process where the areal density of drizzle cells is sufficiently high. The daytime reduction in vertical velocity variance in a less coupled boundary layer is accompanied by enhanced stratification of potential temperature and a buildup of moisture near the surface.

1. Introduction

Large areas of marine stratocumulus clouds form over the subtropical open oceans to the west of continents and underneath the strong capping inversion associated with the descending branch of the Hadley cell. Marine stratocumulus clouds are widespread, low, optically thick, and persist for long periods of time. Their high

albedo allows stratocumulus clouds to reflect large amounts of incoming shortwave radiation. The limited vertical extent of stratocumulus (typical cloud tops are 1–2 km high) means that they emit nearly the same amount of longwave radiation as the underlying ocean. These combined radiative properties have a net cooling effect on Earth's climate (Hartmann et al. 1992). To capture the effects of stratocumulus on large-scale atmospheric circulations, climate models must correctly reproduce the temporal and spatial variability of these clouds, as well as their thickness and height. The radiative properties of stratocumulus remain poorly captured

Corresponding author address: Casey D. Burleyson, North Carolina State University, Box 8208, Raleigh, NC 27695.
E-mail: cdburley@ncsu.edu

in general circulation models (GCMs), constituting a major source of uncertainty in climate simulations (Bony et al. 2006). Cloud-topped boundary layers are notoriously difficult to simulate; the particular deficiencies of various global models have been assessed in numerous studies (e.g., Weare 1996; Bony and Dufresne 2005; Wyant et al. 2006). GCMs often fail to capture the diurnal variation of important processes in the cloud-topped boundary layer system, such as the reduction of cloud fraction and likelihood of decoupling during the afternoon (Abel et al. 2010; Medeiros et al. 2012).

Marine stratocumulus clouds exhibit a particularly strong diurnal cycle because many of the processes that drive turbulent mixing in cloud-topped boundary layers are radiatively forced (Nicholls 1984; Betts 1990; Rogers et al. 1995). In contrast to continental boundary layers, which are usually mixed from the bottom up, marine stratocumulus cloud-topped boundary layers are primarily turbulently mixed from the top down. Buoyancy flux in stratocumulus-topped boundary layers, the maximum of which occurs near cloud top, is the primary source of turbulent kinetic energy (Moeng et al. 1992; Bretherton and Wyant 1997). Parcels near the cloud top become negatively buoyant through a combination of evaporative cooling from the entrainment mixing of warm dry air from the free troposphere and radiative cooling (James 1959). The generation of turbulent kinetic energy by sinking negatively buoyant parcels serves to mix the boundary layer. During the day, some of the cloud-top cooling can be offset by shortwave heating, and the strength of the turbulent connection with the moist subcloud layer diminishes (Nicholls 1984; Turton and Nicholls 1987; Dwyner 1989).

Marine stratocumulus have annual climatological cloud fractions near 70% in the southeast Pacific (SEP) (Klein and Hartmann 1993), and are able to persist for many hours to days. Clouds persist through most afternoons when there is typically net radiative warming. Turbulence connects (or couples) the cloud with the ocean surface and supplies the cloud with moisture. Reduced turbulent mixing can cause the separation of the boundary layer into distinct cloud and subcloud layers, a state called “decoupled” (Turton and Nicholls 1987). In reality, the strength and depth of turbulent mixing in the stratocumulus-topped boundary layer exist in a continuum between fully coupled and fully decoupled. We will refer to the place in the continuum as being more or less strongly coupled. Reduced vertical moisture flux into the cloud when the boundary layer is less strongly coupled means that there is less moisture to offset entrainment or sensible heating, and the cloud can evaporate. If weaker coupling persists, then the cloud

fraction and albedo will decrease as the cloud thins and eventually breaks apart (Betts 1990). Dwyner (1989) showed that the decrease in the degree of coupling between the cloud layer from the surface layer can occur shortly after sunrise and persist until sunset, implying that it takes very little solar heating to reduce the strength of turbulent coupling.

In addition to cloud fraction and the degree of boundary layer coupling, cloud thickness, precipitation, and liquid water path (LWP) also have a regular diurnal cycle. Higher LWP reduces the incoming solar radiation that reaches the surface by modifying the optical depth of the cloud, with thicker clouds absorbing and scattering more incoming radiation. Cloud thickness affects the generation of precipitation (Comstock et al. 2004), which in turn removes liquid water from the cloud and can lead to mesoscale circulations that contribute to the break up the cloud. We will show cycles in precipitation and cloud thickness and how they are related to the diurnal cycle of boundary layer decoupling.

In this study we document the diurnal variation of marine stratocumulus in the SEP with the goal of better understanding the dominant processes that control these climatologically important clouds. The Variability of American Monsoon Systems (VAMOS) Ocean-Cloud-Atmosphere-Land Study Regional Experiment (VOCALS-REx) dataset allows us to examine the diurnal variation of multiple parameters of the stratocumulus-topped boundary layer system simultaneously. To facilitate our understanding of the complex and interrelated processes of the stratocumulus cloud system in the SEP, we examine in concert a multitude of simultaneously measured data from VOCALS-REx. The VOCALS-REx datasets used here are from ship-based instruments (de Szoeke et al. 2010, 2012), each sampling for several weeks across a large cross section of the SEP (Wood et al. 2011). Aircraft studies of the diurnal cycle are limited by the relatively short and temporally sparse nature of the aircraft data. In comparison, the VOCALS-REx ship-based dataset provides a robust diurnal signal. We build on previous work that shows the diurnal cycle in turbulent mixing dominates variability in several of the climatologically important properties of stratocumulus clouds. Our analysis of the diurnal variability of precipitation identifies a new component of the diurnal cycle, a decrease in precipitation in the western portion of the VOCALS-REx domain before the sun comes up, that had previously gone undetected. The observed diurnal cycle can serve as a potential target for future modeling studies attempting to replicate variations in a stratocumulus-topped boundary layer system.

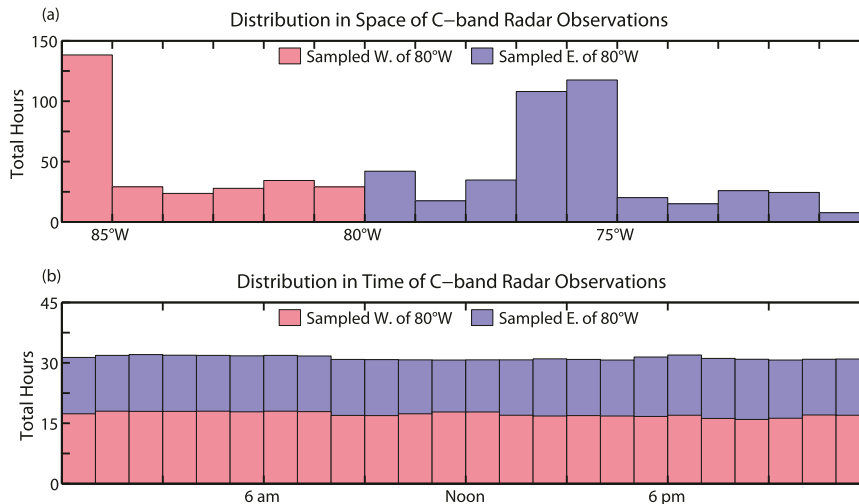


FIG. 1. Distribution of sampling in (a) space and (b) time of hours of C-band radar data collected aboard the *RHB*. Data collected west of 80°W are displayed in pink, whereas data collected east of 80°W are shown in blue.

2. Data and methods

VOCALS-REx data presented here were collected aboard the National Oceanic and Atmospheric Administration (NOAA) research vessel (R/V) *Ronald H. Brown* (*RHB*). The *RHB* traversed the 20°S parallel underneath the SEP cloud deck from Arica, Chile (70°W) to 85°W three separate times during the course of the experiment. Specifically, the two research cruise legs from the ship were from 25 October to 2 November 2008 and from 10 November to 2 December 2008. Along the way, the ship spent several days at each of two ocean buoys moored on the 20°S parallel near 75° and 85°W. The distribution of sampling by the scanning C-band radar (Fig. 1) is representative of sampling by all of the other instruments aboard the *RHB*. The *RHB* samples are temporally continuous and provide a robust picture of the diurnal cycle of the stratocumulus cloud deck. Ship-based data were gathered evenly across the diurnal cycle (Fig. 1). For this reason, we limit our analysis to data obtained aboard the *RHB*.

The *RHB* served as an instrument platform for numerous observations of cloud structure, precipitation, and thermodynamics within the marine boundary layer (de Szoeke et al. 2010). Of primary importance to this study are observations collected utilizing the ship's vertically pointing W-band cloud radar (Moran et al. 2011; de Szoeke et al. 2010, 2012), vertically pointing passive microwave radiometer (Zuidema et al. 2005), scanning Doppler lidar (Grund et al. 2001), scanning C-band precipitation radar (Ryan et al. 2002), laser ceilometer, surface meteorology tower, and the rawinsondes launched every 4 h during the cruise. The *RHB*

was outfitted with a scanning C-band radar to observe light precipitation forming in the shallow stratocumulus clouds. The radar has a wavelength of 5 cm, making it sensitive to moderate drizzle and rain but not the clouds themselves (Ryan et al. 2002). Details of the C-band radar scan strategy used during VOCALS-REx are given in the appendix. The 2- μm high-resolution Doppler lidar (HRDL) measured backscatter intensity and radial wind velocity with 30-m resolution within 6 km of the ship. The scan strategy for the lidar was a repeating 20-min sequence that included plan position indicator (PPI), range-height indicator (RHI), and vertically pointing modes.

One prominent feature of the SEP stratocumulus deck is the gradual increase in boundary layer depth westward from the South American coast in conjunction with warmer underlying sea surface temperatures (Wood and Bretherton 2004; Leon et al. 2008; Zuidema et al. 2009; de Szoeke et al. 2012; among others). In addition, atmospheric aerosol concentrations have also been observed to decrease westward, resulting in a longitudinal gradient in cloud droplet number concentrations (Bennartz 2007; Wood et al. 2008; George and Wood 2010; Bretherton et al. 2010). There is synoptic and interannual variability in the longitudinal gradients of these properties, yet the gradients were observed most times during VOCALS-REx. Both boundary layer depth and cloud droplet number concentration have been shown to interact with the cloud-aerosol-precipitation processes in the stratocumulus clouds over the SEP, resulting in longitudinal gradients in drizzle and cloud fraction (Wood and Bretherton 2004; Leon et al. 2008; Mecham et al. 2012). The time series of data from the

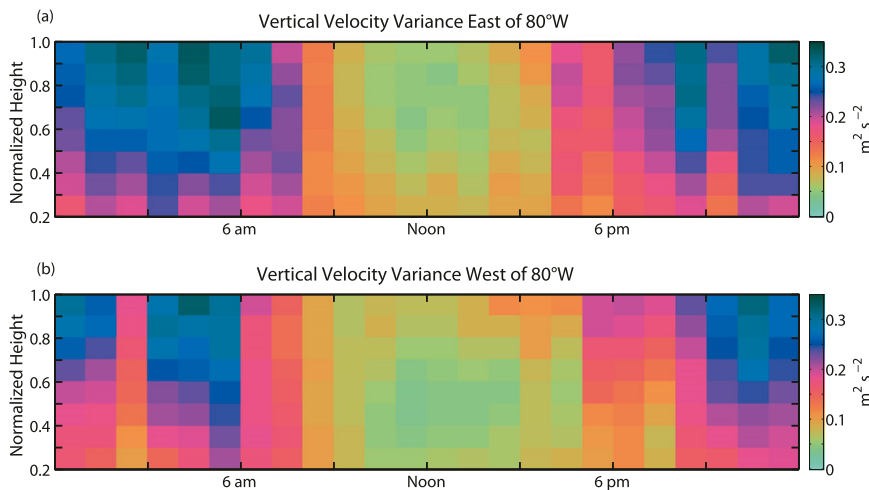


FIG. 2. Time–height profiles of the mean vertical velocity variance in the boundary layer for the region (a) east and (b) west of 80°W using data from the vertically pointing Doppler lidar. The profiles are normalized to the base of the cloud, such that a height of 1.0 represents the base of the cloud and a value of 0.2 represents a height that is 20% of the measured cloud-base height. Individual data points with an SNR greater than 15 dB are removed to limit the influence of precipitation on the turbulence statistics.

ship (e.g., de Szoeke et al. 2010, their Fig. 2) does show diurnal, longitudinal, and synoptic variability, with the dominant signals in the time series being the diurnal and longitudinal patterns. To account for longitudinal variability in our analysis of the diurnal cycle, we have subdivided our results into two regions, east and west of 80°W , when sample sizes allow it. Subdividing the data in this way isolates the effects of the longitudinal gradients in cloud properties from the diurnal cycle. Throughout the paper, results shown in blue represent data collected in the region east of 80°W (i.e., closer to the coast, higher aerosol concentration, shallower boundary layer) and results shown in pink represent data west of 80°W (i.e., farther from the coast, lower aerosol concentration, deeper boundary layer).

The relatively slow motion of the ship compared to the evolution time of the atmosphere means that the *RHB* was subject to synoptic influences in the region [see Toniazzo et al. (2011) for a discussion of the synoptic meteorology conditions in the southeast Pacific during VOCALS-REx]. Synoptic variability in key variables is smaller along and north of 20°S compared to regions closer to the extratropical cyclone track farther south. For example, the variability of inversion height associated with synoptic influences is roughly $\pm 0.2\text{--}0.4\text{ km}$ along 20°S compared to $\pm 0.8\text{--}1.0\text{ km}$ along 30°S (Toniazzo et al. 2011, their Fig. 21a). There is no reason to believe that the synoptic forcing will systematically occur at any one time during the diurnal cycle. Rather, synoptic influences will show up as small random perturbations on top of the mean diurnal cycle that comes from 31 days of data.

We examine both the mean and quartiles of several variables to capture their underlying distribution and avoid possible misinterpretation that may arise from taking averages of a non-Gaussian distribution (Taleb 2007). The hourly mean values in our analysis will be indicated by a thick line, overlaid on a shaded region that indicates the area between the 25th and 75th percentiles of the hourly distributions. While most of the distributions appear to be quasi Gaussian, with the mean lying approximately in the middle of the interquartile range, precipitation intensity and drizzle cell size are lognormal. All times given have been converted to local solar time using the longitude at which the measurement was made.

3. Results

a. Boundary layer mixing

We begin an analysis of the diurnal cycle by examining factors controlling the diurnal variation of boundary layer mixing. Our analysis focuses on the diurnal cycle of boundary layer mixing and stratification and complements recent studies of the diurnal cycle of stratocumulus in the southeast Pacific (de Szoeke et al. 2012; Painemal et al. 2013). Figure 2 shows a time–height representation of the vertical profile of mean vertical velocity variance measured from the NOAA high-resolution Doppler lidar. Data were collected in 10-min windows when the lidar was in vertically pointing mode. The mean profiles were normalized to the base of the

cloud such that a height of 1.0 represents cloud base, while 0.2 represents a height that is 20% of the measured cloud-base height. The data were quality controlled using the signal-to-noise ratio (SNR) to remove weak signals ($\text{SNR} < 0\text{ dB}$) and the downdrafts associated with precipitation ($\text{SNR} > 15\text{ dB}$). Higher variance of the vertical velocities indicates stronger turbulent mixing.

Consistent with a mixing profile that is driven by top-down mixing (James 1959), the strongest variance values are located at the base of the cloud and top of the subcloud layer and variance decreases downward toward the surface. The diurnal cycle of boundary layer mixing is evident both east and west of 80°W . Overnight mean profiles have higher vertical velocity variance compared to the midday values. Shortly after sunrise ($\sim 0600\text{ LST}$) the variance values decrease sharply throughout the depth of the subcloud layer as solar heating acts to limit the generation of negatively buoyant parcels at cloud top. Vertical velocity variance remains low throughout the day and begins to slowly increase again as the sun goes down ($\sim 1800\text{ LST}$). Overall, turbulent mixing is somewhat stronger and deeper in the east (Fig. 2a) compared to the west (Fig. 2b). This is consistent with a boundary layer that is shallower and more strongly coupled closer to the coast compared to farther away. We believe the anomalous values of vertical velocity variance between 0200 and 0300 LST west of 80°W are likely an artifact because of a combination of the large variability of conditions at that time and small sample size of the vertically pointing lidar data.

One interesting feature of this analysis is the rate at which turbulence decreases after sunrise compared to the rate at which it increases after sunset. There is a distinct decrease in the mean vertical velocity variance profiles after 0800 LST in both the eastern and western portions of the VOCALS-REx domain. This indicates a sudden reduction in the overall strength of the turbulent motions. The pace at which turbulence begins to strengthen after sunset is much slower. Strong turbulent overturning is not present until roughly 1900–2000 LST in the east and after 2100 LST in the west. Because the generation of turbulence via longwave cooling is amplified by the presence of cloud, this delay in the strengthening of turbulent mixing could be due to the time after sunset that it takes for the cloud fraction to increase to its overnight values. Previous work has shown that it takes several hours after sunset for cloud fraction to recover to its overnight value (de Szoek et al. 2012, their Fig. 8a).

We used the 4-hourly VOCALS-REx sounding data to construct mean profiles of potential temperature, water vapor mixing ratio, and horizontal wind speeds. In

this case we did not divide the data into east and west regions because of the smaller sample size of the 216 radiosonde launches. To account for the east–west gradient in boundary layer depth, we normalize the height coordinate to the base and top of the cloud. The subcloud layer in each sounding is divided into 10 evenly spaced bins that span the height between 50 m above the surface and the measured base of the cloud, and within the cloud 5 bins are evenly distributed between the measured cloud base and cloud top. Figure 3a shows the diurnal cycle of average potential temperature between 50 m above the surface and the top of the cloud. Where potential temperature is constant with height, the temperature gradient is neutrally stable to adiabatic motions of unsaturated air parcels.

One salient feature of Fig. 3a is the nearly isentropic layer ($\sim 290\text{ K}$) formed shortly after sunset ($\sim 1800\text{ LST}$) from the surface up halfway to cloud base. Between midnight and 0400 LST, this nearly isentropic layer extends farther upward to encompass the full vertical extent of the subcloud layer. This indicates strong upward and downward mixing. Negatively buoyant cloud parcels may descend toward the surface without encountering a stable layer. Likewise, positively buoyant subcloud parcels would encounter no strong stability boundaries during their ascent to cloud base. The projection of this vertical overturning onto the horizontal winds may also be the cause of the high wind speeds in the subcloud layer overnight (Fig. 3c). The sun rises between the 0400 and 0800 LST sounding and there is a 1-K cooling throughout most of the subcloud layer, with the strongest cooling occurring in the lowest third of the subcloud layer. Cooling of the subcloud layer in the early morning hours is likely a sign of radiatively cooled parcels from cloud top being mixed downward into the subcloud layer. Evaporative cooling from drizzle could also be contributing to the observed cooling. More importantly though, during this period around sunrise the vertical potential temperature gradient also begins to increase, indicating a stable layer between cloud base and the surface. Between 0800 and noon LST a layer just below cloud base becomes more strongly stable, with a vertical potential temperature gradient greater than 1 K between cloud base and the surface. Horizontal wind speeds on top of the stably stratified layer decrease while remaining fairly steady within the mixed layer extending upward from the surface. The increased stratification of potential temperature during the morning and afternoon would inhibit the availability of surface moisture to the cloud.

To investigate the effect of increased stability on the moisture, we calculated the water vapor mixing ratios (g kg^{-1}) using temperature and relative humidity data

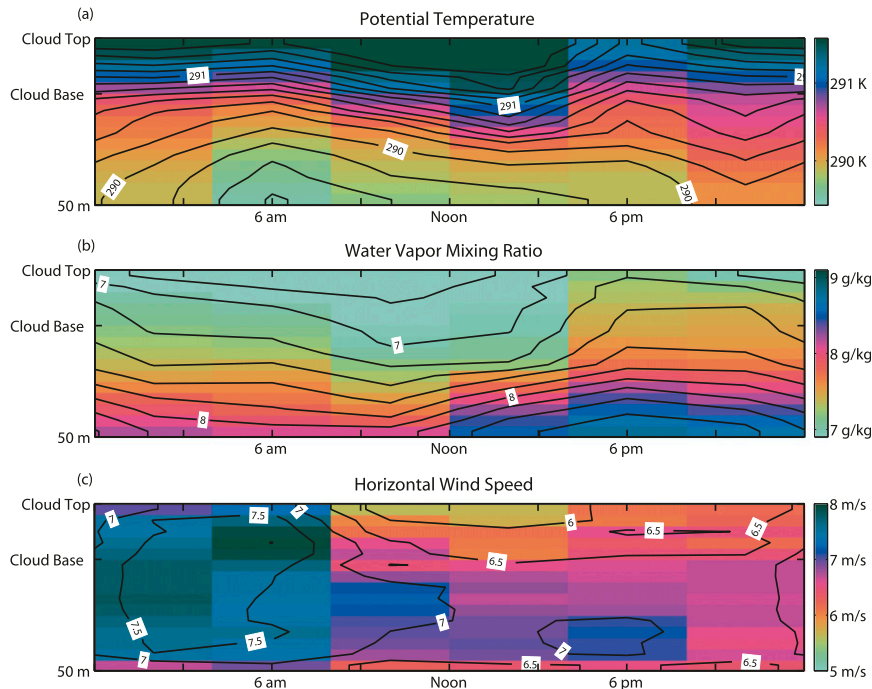


FIG. 3. 4-h averages of the vertical profiles of (a) potential temperature, (b) water vapor mixing ratio, and (c) horizontal wind speed from the soundings launched from the *RHB*. The profiles use LST and are normalized to the base and top of the cloud to capture the relative heights of boundary layer–mixing properties. The contour intervals are 0.15 K for potential temperature, 0.2 g kg^{-1} for water vapor mixing ratio, and 0.5 m s^{-1} for wind speed.

from the soundings. We use the water vapor mixing ratio as a conserved tracer to indicate the vertical extent of moisture in the boundary layer. Surface evaporation rates are roughly constant across the diurnal cycle (de Szoeke et al. 2010), so the diurnal variation in moisture content near the surface is a function of the rate at which moisture is transported away from the surface. The average water vapor mixing ratio profiles shown in Fig. 3b illustrate the diurnal variation of the degree of coupling of the boundary layer. Drying in the layer immediately beneath cloud base begins after sunrise and slowly extends downward toward the surface. During the day, a clearly defined moist surface layer forms when the cloud deck is generally less well coupled with the surface. Moisture in the lower portion of the subcloud layer increases in time after noon. The interface between the dry subcloud layer and the surface-based moist layer creates a strong vertical gradient in the water vapor mixing ratio. Water vapor near the surface reaches its diurnal maximum ($\sim 9\text{ g kg}^{-1}$) by sunset. Vertical moisture gradients decrease after sunset as moisture is again mixed upward away from the surface, resulting in a more evenly distributed moisture profile. This process allows the cloud to tap into the reservoir of surface moisture, resulting in a deeper stratocumulus cloud deck and higher cloud fractions overnight.

The mean sounding data indicate a fairly regular daily transition in the degree of coupling in the stratocumulus-topped boundary layer system. We can visualize one example of this transition using lidar data collected on 2 November 2008 (Fig. 4a). The strongest scattering of the lidar beam occurs within the cloud deck and during drizzle where signal strength values upward of 20 dB occur. Aerosols have weaker backscatter than cloud and are present in varying concentrations from cloud base to the ocean surface. Aerosol backscatter intensity is a function of number concentration and size of the scatterers. Higher ambient relative humidity also increases the lidar backscatter by swelling hygroscopic particles (Tang, 1996). From 0400 through 1100 LST, aerosols in the subcloud layer are vertically well mixed and their corresponding backscatter intensity is roughly constant from the ocean surface to the cloud base (Figs. 4a and 4b). Shortly after local noon, a cleaner (lower aerosol concentration) or drier (lower relative humidity) layer with lower backscatter begins to appear below cloud base and grows downward to eventually encompass almost half of the subcloud layer by sunset. The gradient in aerosol backscatter between the dirty and/or moist near-surface layer and the cleaner and/or drier air above represents the top of the well-mixed surface layer

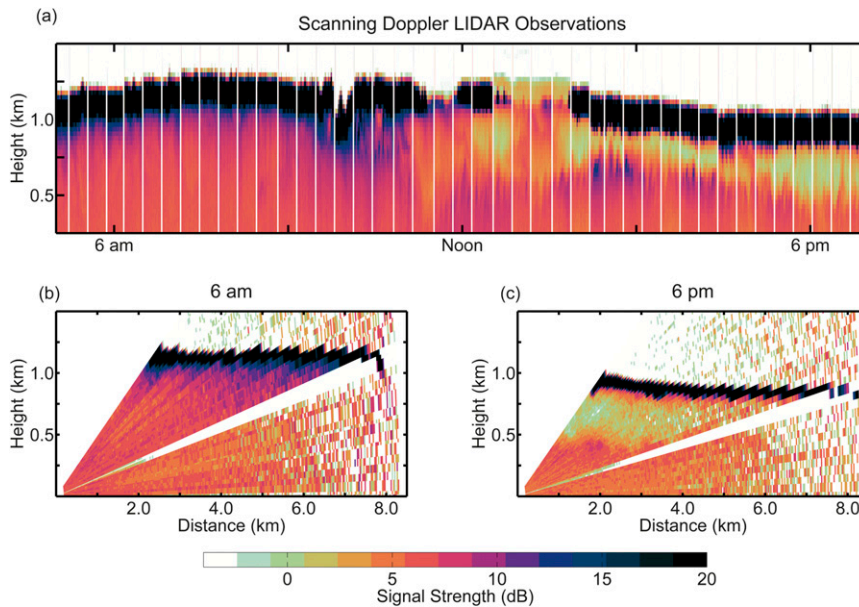


FIG. 4. Time–height variation of range-corrected backscatter intensity from (a) a vertically pointing Doppler lidar aboard the *RHB*, and select RHI scans from the lidar at (b) 0600 and (c) 1800 LST. Data shown were collected on 2 Nov 2008 near 19.6°S, 74.8°W. The 10-min blocks of vertically pointing data, obtained every 20 min, are plotted close together to make the figure easier to display.

during the period when there is a decoupled boundary layer (Fig. 4c).

b. Surface variables

Hourly 10-m surface air temperature values are shown in Fig. 5a. As expected in a cloud-topped marine boundary layer, the diurnal variation in air temperature is quite small (less than 1°C both east and west of 80°W). Daily minimum values occur near sunrise, followed by a gradual increase throughout the morning that peaks around local noon. The air temperatures after noon remain fairly constant for a period of 10–12 h and then gradually decrease in the overnight hours. The high cloud fraction of the stratocumulus deck and large heat capacity of the underlying ocean play a significant role in the moderation of the daily temperature cycle. A minimal temperature difference between the ocean and the lower atmosphere (typically 1°–2°C; Painemal et al. 2010) limits the exchange of sensible heat from the ocean to the atmosphere (<6 W m⁻²; de Szoeke et al. 2010). The mean air and sea surface temperatures in the western portion of the SEP stratocumulus domain are about 1°C warmer than the eastern portion (Bretherton et al. 2004).

Diurnal variation in near-surface dewpoint temperature is shown in Fig. 5b. Dewpoints have a diurnal minimum near local sunrise, increase roughly linearly until just before local sunset, and then gradually drop. The amplitude of the diurnal variation is close to 1.5°C

in both the east and west, and its sinusoidal pattern follows that of temperature from midnight to noon LST, when the boundary layer is more coupled. When the boundary layer becomes less coupled in the afternoon, the dewpoint temperature rises because of the increase in moisture content of the near-surface boundary layer. Surface moisture accumulates during the day when the coupling with the cloud deck is weakest and decreases overnight because of stronger vertical moisture fluxes away from the surface.

Near-surface wind speed and wind direction distributions across the diurnal cycle are shown in Figs. 5c and 5d. There is only a weak cycle near surface wind speeds. The magnitude of the wind speed longitudinal gradient is larger than the diurnal variability. There is a 2 m s⁻¹ difference in hourly mean wind speed between the east and west compared to a 1.2 m s⁻¹ between maximum and minimum hourly mean wind speed in both the east and west. Mean wind direction in the western portion of the VOCALS-REx domain shows little diurnal variability, while in the eastern portion there is a persistent backing of the near-surface winds from southeast to east-southeast during the day. This change in wind direction is consistent with the documented coastal meteorology patterns along the western coast of South America (Garreaud and Muñoz 2004).

The diurnal distributions of downwelling shortwave and longwave radiative flux, measured at 10-min

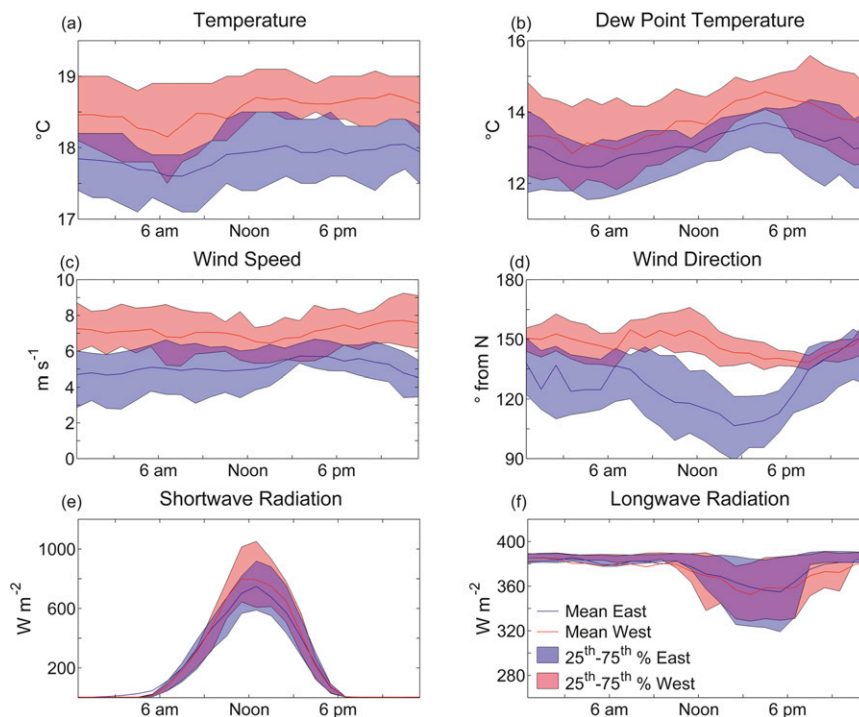


FIG. 5. Hourly mean (solid line) and interquartile range (shaded region) of the (a) near-surface air temperature, (b) dewpoint temperature, (c) wind speed, (d) wind direction, (e) incoming shortwave radiation, and (f) incoming longwave radiation from an upward-pointed sensor, plotted as a function of LST for regions east and west of 80°W.

intervals, are shown in Figs. 5e and 5f, respectively. The underlying distribution of shortwave radiation has a positive definite cosine shape with a daily maximum mean value near local noon in both the west ($\sim 800 \text{ W m}^{-2}$) and east ($\sim 700 \text{ W m}^{-2}$). Previous studies have shown that the western cloud field tends to break up earlier and more often than in the eastern region closer to South America (Bretherton et al. 2010). The larger interquartile range of shortwave radiation in the western portion of the domain indicates a less consistent cloud field. Not surprisingly, downwelling longwave radiation is strongest and most consistent ($\sim 380 \text{ W m}^{-2}$) at night, when the cloud is thickest and most spatially coherent. The afternoon minimum mean value and the larger interquartile range in both regions ($\sim 360 \text{ W m}^{-2}$) are related to cloud break up. While the extrema of the mean diurnal cycle in downwelling longwave radiation are similar throughout the VOCALS-REx domain, the range in the distribution increases slightly earlier and decreases slightly later west of 80°W. This is consistent with a cloud deck that breaks up slightly earlier and reforms slightly later in the west compared to the east. While the mean values of the ship's longwave radiative flux measurements are consistent with those from the C-130, the limited diurnal sampling of the aircraft data misses some of the subtlety of the diurnal

cycle, such as the increased variability in the western half of the domain (Bretherton et al. 2010).

Sulfate is the dominant submicron aerosol species in the VOCALS-REx region (Jaeglé et al. 2011; Shank et al. 2012), and the diurnal variation in its gas-phase precursors peaks overnight west of 78°W (Yang et al. 2011). Near-surface aerosol concentration observations were made at the bow of the ship ($\sim 15 \text{ m}$ above sea level) during VOCALS-REx. The near-surface concentrations of Aitken and accumulation mode aerosols—roughly less than and greater than $0.1 \mu\text{m}$ in diameter, respectively—were measured at 10-min intervals. There is large day-to-day and week-to-week variability in the measured near-surface aerosol concentrations. The hourly means and interquartile ranges of these concentrations are shown in Figs. 6a and 6b. Aerosol concentration varies for some individual days and is relatively constant for others. Consistent with previous work, we found no robust or systematic diurnal cycle in aerosol concentrations (Tomlinson et al. 2007). There was a longitudinal gradient in aerosol concentrations with higher concentrations in the east (e.g., Allen et al. 2011; de Szoeke et al. 2012). The mean near-surface accumulation mode aerosol concentration east of 80°W was about 50 cm^{-3} higher than in the west. In the

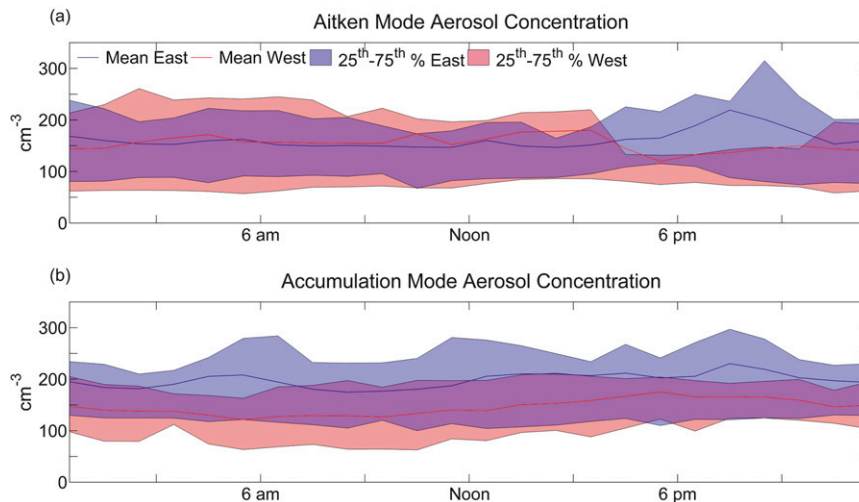


FIG. 6. Hourly mean and interquartile range of near-surface aerosol concentrations for aerosols (a) smaller than $0.1\text{-}\mu\text{m}$ diameter (roughly Aitken mode) and (b) larger than $0.1\text{-}\mu\text{m}$ diameter (roughly accumulation mode) for regions east and west of 80°W .

Aitken mode, a weak east-to-west gradient of about $50\text{--}100\text{ cm}^{-3}$ occurs only during the afternoon and early evening. Whether the afternoon and early evening variation reflects changes in formation or scavenging is unclear.

c. Cloud measurements

As with other variables, variations in the base and top of the cloud are affected by the diurnal cycle. During VOCALS-REx several instruments were deployed to measure changes of the height and depth properties of the cloud (de Szoek et al. 2012). The east–west division

allows the diurnal variability to be compared with longitudinal variability. Diurnal variations in the base of the cloud are shown in Fig. 7a. Shortly after sunrise, the mean altitude of cloud base begins to increase, rising approximately 200 m by noon in both the eastern and western portions of the domain. After noon, the base of the cloud lowers until it reaches its overnight value by sunset, at which point the cloud base remains fairly steady throughout the night. One significant feature of the measured cloud-base heights is the distinct east–west difference. Cloud bases in the western portion of the domain are on average 200 m higher than those closer to the coast.

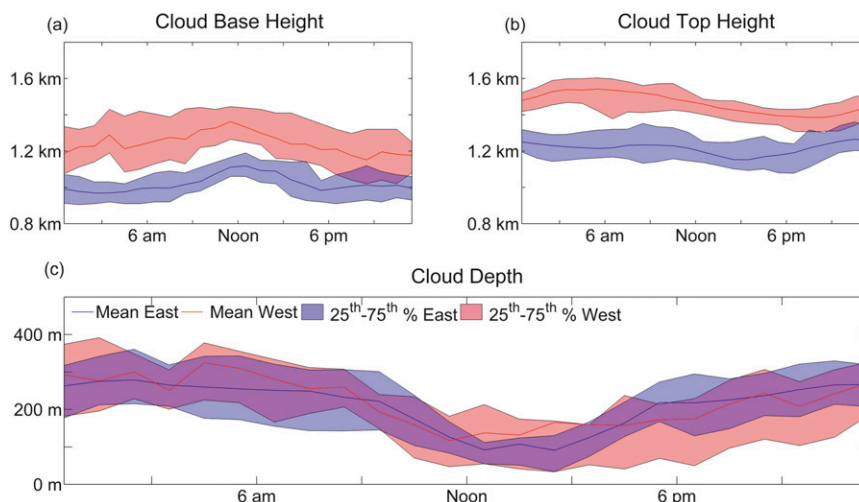


FIG. 7. Hourly mean and interquartile range of (a) cloud-base heights measured by the laser ceilometer, (b) cloud-top heights measured by interpolating the inversion height measured by the soundings taken every 4 h, and (c) the resultant depths of the cloud for regions east and west of 80°W .

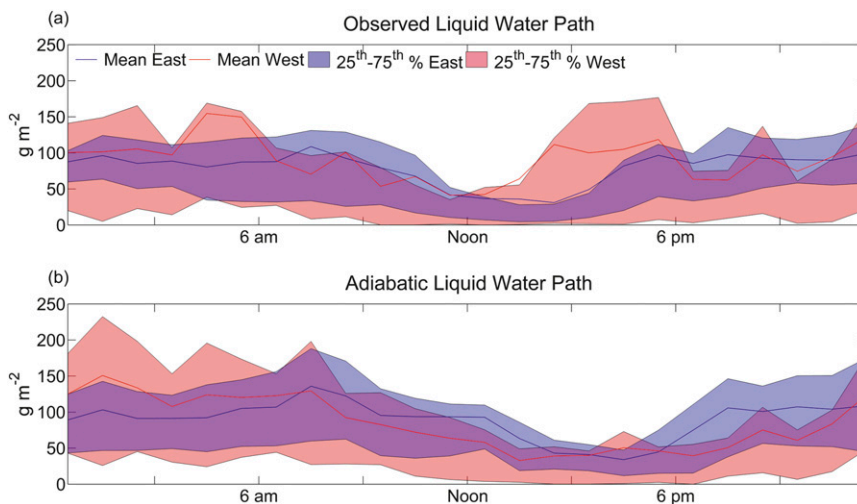


FIG. 8. Hourly mean and interquartile range of (a) the observed LWP and (b) the adiabatic LWP computed from the cloud-base and height measurements for regions east and west of 80°W .

The top of the stratocumulus cloud deck, Fig. 7b, coincides with the height of the subsidence inversion. Inversion base height was measured every 4 h from the soundings launched from the ship. In this study, the top of the cloud is estimated from the inversion height from soundings and interpolated from the soundings to every 10 min. This method of determining the stratocumulus cloud-top height is consistent during both legs of VOCALS-REx and agrees well with the measurement from the vertically pointing W-band radar when it was available during the second leg. The strong east–west gradient of boundary layer depths manifests itself in higher cloud tops westward. Farther west from the coast, the height of the inversion is nearly 250 m higher than in the eastern portion of the VOCALS-REx domain. Cloud-top heights also show a significant diurnal variation. Discounting horizontal advection in the boundary layer, the height of the subsidence inversion will increase because of entrainment into the boundary layer of warm dry air from above the inversion and decrease because of subsidence of air above the inversion. For the 10 h from midnight through 1000 LST, these two counteracting tendencies are balanced and the cloud-top height is fairly constant east of 80°W . Overnight the cloud-top height increases to its maximum altitude around midnight in the east and closer to 0300 LST in the west. As the cloud begins to break up after sunrise, the rate of subsidence outpaces entrainment deepening, causing the boundary layer to become shallower (Lewellen and Lewellen 1998). By 1800 LST, the mean cloud top west of 80°W has decreased nearly 150 m from its overnight value. In the east, the decrease in cloud-top height

is between 75 and 100 m. A shallower boundary layer persists until the cloud begins to recover near sunset and entrainment warming and deepening are able to overcome subsidence.

Overnight the cloud depth is nearly constant as a result of stationary cloud-base and cloud-top heights. Mean cloud depths are close to 300 m, with only slightly deeper clouds in the western portion of the domain compared to the east. After sunrise, increasing cloud-base heights combine with a steady cloud top to decrease the cloud depth by a factor of 2 by early afternoon. The mean rate of thinning ($\sim 25 \text{ m h}^{-1}$) is constant throughout the morning. The cloud gradually thickens after 1500 LST. The 9 h it takes for the cloud to thicken (at $\sim 15 \text{ m h}^{-1}$) to its nighttime value is somewhat slower than the time it takes to thin. These rates are consistent with a boundary layer that takes longer to recouple than decouple (Fig. 2).

As southeast Pacific stratocumuli are largely adiabatic (Zuidema et al. 2012), the diurnal cycle of liquid water path (Figs. 8a and 8b) very closely resembles the diurnal cycle in cloud depth. Liquid water path values are at times positively skewed such that the mean is closer to the 75th percentile than the 25th percentile. Further discussion of the liquid water path characteristics for the region, including diurnal and longitudinal gradients in adiabaticity, is given in de Szoeke et al. (2012) and Zuidema et al. (2012).

d. Precipitation

Drizzle frequently forms in shallow stratocumulus clouds as a result of collision and coalescence of cloud

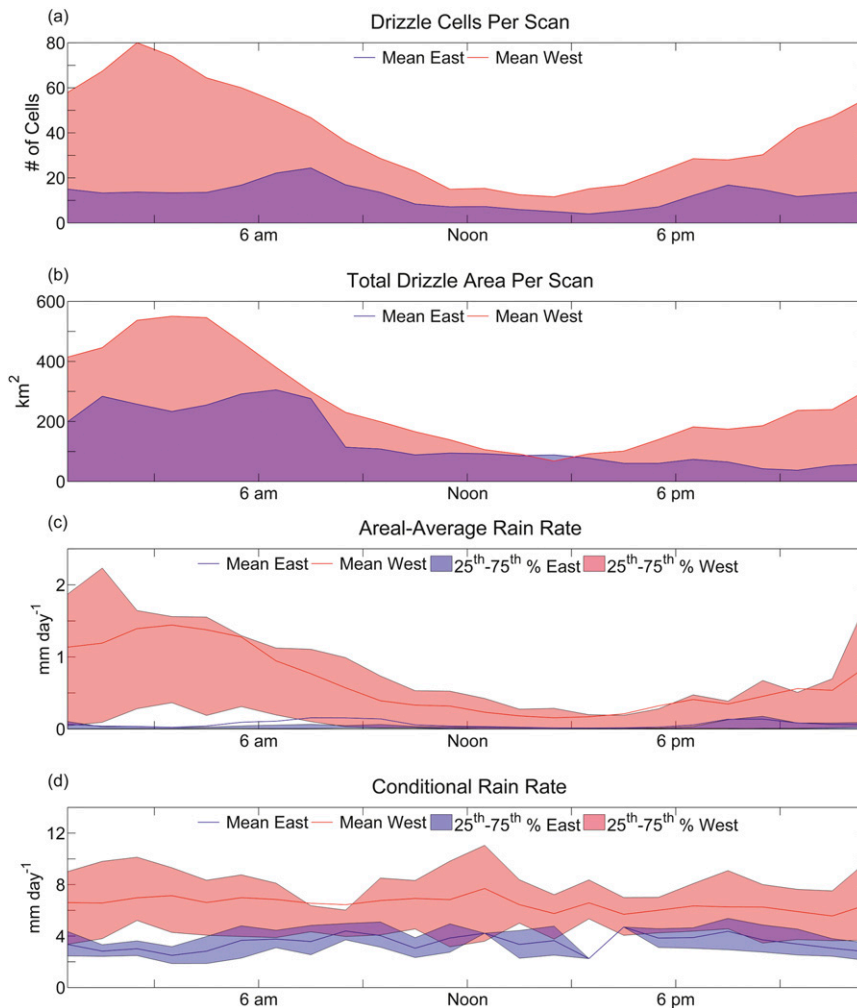


FIG. 9. Diurnal variation of the (a) mean number of drizzle cells per scan, (b) mean total precipitation area per scan, (c) mean (solid line) and interquartile range (shaded region) of the hourly areal-average rain rate, and (d) mean (solid line) and interquartile range (shaded region) of the hourly conditional rain rate, derived from measurements from the scanning C-band precipitation radar aboard the *RHB*.

droplets. When present, drizzle often organizes into discrete cellular structures, with cloud tops over drizzling cells being slightly higher than the areal-averaged cloud-top height (e.g., vanZanten and Stevens 2005; Comstock et al. 2005, 2007). Drizzle formation, fallout, and cessation are dependent on many factors, such as cloud-base and cloud-top height, cloud depth and liquid water content, cloud-aerosol interaction, and boundary layer turbulent moisture transport (e.g., Comstock et al. 2004, 2005; Zuidema et al. 2009). To determine drizzle cell frequency and extent, we follow Comstock et al. (2007) and use an algorithm designed to look for contiguous regions of radar reflectivity greater than 5 dBZ. This algorithm separates individual drizzle cells from the background cloud. Relaxing the minimum reflectivity

threshold to 0 dBZ, a commonly accepted threshold for drizzle that is likely reaching the surface (Comstock et al. 2004), slightly modifies the drizzle cell-size distributions (shown in Fig. 10) but does not otherwise affect our results. We used a minimum cellarea threshold of just over 0.5 km², which corresponds to eight contiguous radar pixels. The diurnal mean values for the number of drizzle cells observed in each radar scan and the cumulative drizzle area for regions both east and west of 80°W are shown in Figs. 9a and 9b.

The diurnal maximum of cell counts and total precipitation area (Figs. 9a and 9b) is between midnight and sunrise, when the cloud is thickest. During the night, the C-band radar observed over 3 times the number of drizzle cells in the region west of 80°W than in the region

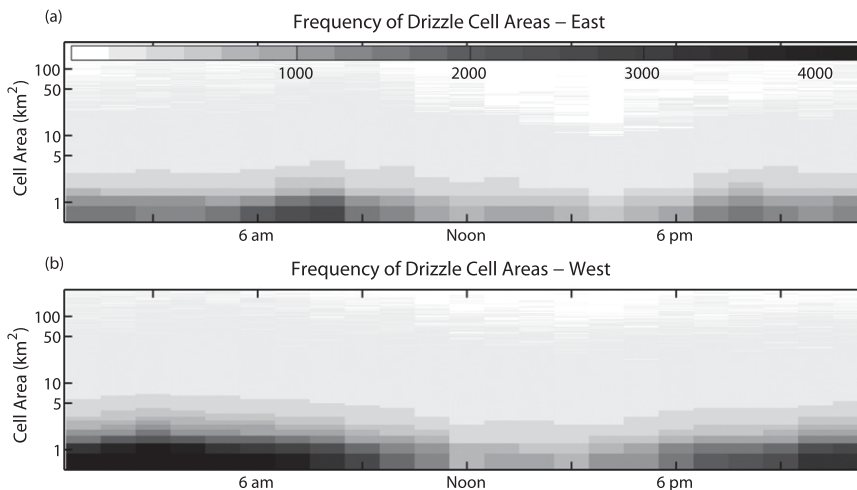


FIG. 10. Distribution of drizzle cell areas for all precipitation observed during VOCALS-REx for the regions (a) east and (b) west of 80°W . The vertical axis is on a logarithmic scale.

east of 80°W . The enhanced drizzle frequency in the west is consistent with the deeper boundary layer, slightly higher LWP, and fewer cloud condensation nuclei in the environment west of 80°W . Figure 9c shows the diurnal mean and distribution of areal average rain rates for both regions of the VOCALS-REx domain. The areal average rain rates east and west of 80°W are broadly consistent with the gradients documented in the C-130 and *CloudSat* data (Bretherton et al. 2010). The cloud-base rain rate for drizzling stratocumulus clouds is proportional to the cloud depth and LWP (e.g., Comstock et al. 2004). The hourly conditional rain rate (Fig. 9d) is the average of raining pixels (those above a range-dependent sensitivity threshold) for all hours in which the precipitating area exceeded 100 km^2 (see the appendix for details). In the region west of 80°W , the mean conditional rain rate was 6.5 mm day^{-1} compared to 3.5 mm day^{-1} east of 80°W . The conditional rain rates for the east and west regions each show very little diurnal variation. The diurnal variation of the areal average rain rates for a given region is primarily related to variations in the drizzling area rather than changes in the intensity of drizzle.

The size distribution of all individual drizzle cell areas observed by the C-band radar during VOCALS-REx (Fig. 10) is highly skewed, and drizzle cells with areas smaller than 1 km^2 outnumber cells of larger sizes throughout the diurnal cycle. The increase in the overall number of drizzle cells overnight (Fig. 9a) is related to both a large increase in the number of smaller drizzle cells and more larger cells (broadening the cell area distribution). West of 80°W , the number of drizzle cells smaller than 1 km^2 nearly quadruples, from 1800 to 0300 LST.

The extensive VOCALS-REx radar dataset provides a clear view of how drizzle varies diurnally, but it also brings to light an important contrast in the timing of precipitation between the eastern and western portions of the VOCALS-REx domain. The timing of changes in the mean total area of precipitation east of 80°W is closely tied to sunrise and sunset. The total area of C-band-observed precipitation decreases from about 250 to about 100 km^2 , from a radar coverage area of roughly $10\,000\text{ km}^2$, between 0700 and 0900 LST (Fig. 9b). This decrease in precipitation occurs as the cloud thins and turbulent moisture transport begins to weaken after sunrise. The number of drizzle cells and the total drizzle area remain small throughout the day. Once the turbulent vertical moisture flux increases again after sunset, the precipitation area increases to its overnight value. In contrast, west of 80°W the maximum precipitation area occurs between 0300 and 0500 LST, and begins to decrease before the sun comes up. In the predawn hours, the solar radiation has yet to reduce turbulence generation and vertical moisture transport, so it cannot yet affect the cloud and precipitation. The reduction in the number of drizzle cells, the total drizzle area, and the areal-average rain rate is out of phase with the diurnal variations in cloud thickness, liquid water path, and boundary layer turbulent mixing, indicating a different process limits drizzle in the early morning hours in the western region of the VOCALS-REx domain.

We examined several potential reasons for the decrease in precipitation between 0300 and 0500 LST in the western portion of the domain. The cloud itself is generally persistent. Figure 7 shows that the cloud base, cloud top, and cloud depth in the western portion of the domain are all roughly constant between midnight and

0600 LST. Liquid water path measurements (Fig. 8) have a higher mean ($\sim 150 \text{ g m}^{-2}$) and are more positively skewed between 0300 and 0600 LST compared to the window between midnight and 0300 LST. The impact of the “upsidence” wave, modeled by Garreaud and Muñoz (2004, their Fig. 5) and Rahn and Garreaud (2010, their Fig. 14), is inconclusive in the western portion of the VOCALS-REx domain in the 3–6 h before sunrise. The free-tropospheric subsidence anomaly is either neutral or slightly negative (upward). Wood et al. (2009, their Figs. 5a and 6) found that the region west of 80°W should have a diurnal minimum in subsidence and a higher mean liquid water path in the 6 h before sunrise. Their work was based on European Centre for Medium-Range Weather Forecasts (ECMWF) analyses and passive microwave data. The modeling work of Wyant et al. (2010) showed LWP and cloud fraction changed little because of the upsidence wave in the SEP stratocumulus deck. If anything, the higher liquid water paths associated with the upsidence wave would increase precipitation, in contrast to the observed decrease in precipitation. Therefore, we believe that the upsidence wave is likely not the cause of the observed decrease in precipitation in the early morning hours over the western portion of the VOCALS-REx domain.

Another possible explanation for the early morning diminution of the number of drizzle cells and the areal average rain rate west of 80°W is that the precipitation itself causes a reduction in the vertical moisture transport by creating a stability boundary in the subcloud layer (Bretherton and Wyant 1997). A majority of the drizzle from marine stratocumulus clouds evaporates before reaching the surface and this evaporation will drive cooling in the subcloud layer (Comstock et al. 2004). Evaporative cooling of the subcloud layer can generate a stable lapse rate beneath the base of the cloud [e.g., the “drizzling” potential temperature profiles of Comstock et al. (2005)]. Jones et al. (2011) show that higher cloud-base and LCL height differences, a symptom of less coupled boundary layers, are correlated with times of heavier drizzle. This relationship was particularly evident farther from the coast, where heavier drizzle is most prominent.

A possible example of the near-cloud-base precipitation-induced stabilization is shown in Fig. 11, where we compare two soundings launched roughly 5 h apart on 23 November 2008 when the ship was near 85°W . Drizzle was in the vicinity of the ship for the entire time between the two soundings. In the 2145 LST sounding (Fig. 11a), the subcloud potential temperature profile is isentropic all the way up to the base of the cloud. The subsequent sounding at 0230 LST (Fig. 11b), launched after persistent drizzle was in the vicinity of the ship for many hours,

shows a potential temperature profile that increases upward from 0.9 km to cloud base at 1.2 km. This slight stability boundary could be enough to inhibit vertical moisture transport into the cloud and limit further precipitation.

It is our hypothesis that the total area of drizzle cells is self-limiting. Vertical mixing can be reduced by localized evaporative cooling and stabilization related to drizzle from individual small drizzle cells even if a detectable cold pool does not form. The combined effect of a high areal density of these small cells over time is to limit opportunities for new cells to form. Only a subset of drizzle cells are strong enough to produce sufficiently negatively buoyant air from evaporative cooling to yield surface cold pools and hence opportunities for surface convergence and new cell growth (vanZanten and Stevens 2005; Feingold et al. 2010; Terai 2011). We are not proposing that the entire domain would be stabilized by precipitation, which is unlikely given the areal average rain rates of 1.5 mm day^{-1} or less. Rather, the ensemble of cell local stabilization effects near cloud base, such as illustrated by the soundings in Fig. 11, may yield a domainwide phenomenon that manifests as a statistical decrease in the number of drizzle cells, the total precipitation area, and the areal average rain rates (Figs. 9 and 10).

The drizzle-induced reduction in vertical mixing mechanism builds on previous studies of drizzle processes in marine stratocumulus, namely, Wang and Wang (1994), Bretherton and Wyant (1997), and Wang and Feingold (2009). This postulation also allows that the upsidence wave may indirectly contribute to the noticeable precipitation decline by enhancing the ability of the cloud to precipitate, thus speeding up the rate of subcloud evaporative cooling and stabilization, which subsequently reduces the precipitation after 0300 LST. Untangling this sequence of events will require further study.

4. Conclusions

We used observations collected aboard the *RHB* during VOCALS-REx to investigate diurnal variations in the marine stratocumulus cloud deck over the SEP. We use coincident observations of boundary layer thermodynamics, cloud properties, and drizzle to identify processes that determine the state of the stratocumulus-topped boundary layer. The high temporal and spatial continuity and the large sample sizes provided by the *RHB* data allow us to resolve the diurnal transition in the degree of coupling of the stratocumulus-topped boundary layer. A conceptual schematic for the diurnal variation of marine stratocumulus clouds, surface mixed-layer depth, drizzle, and boundary layer mixing in the

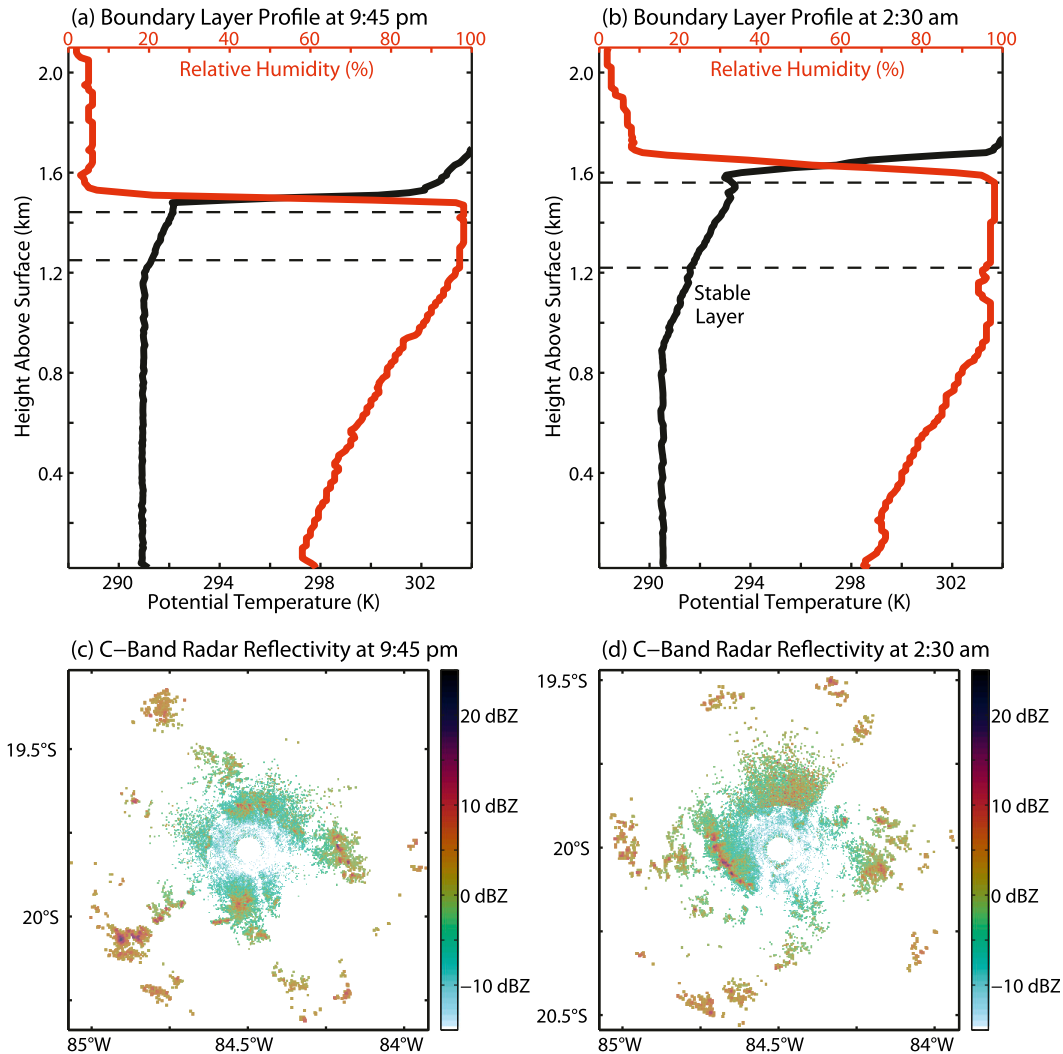


FIG. 11. Boundary layer profiles of potential temperature (black lines) and relative humidity (red lines) measured by consecutive atmospheric soundings launched at (a) 2145 LST 22 Nov and (b) 0230 LST 23 Nov 2008. Horizontal dashed black lines show the approximate boundaries of the cloud at the time that the measurement was taken. The soundings were launched from the *RHB* while it was stationed at roughly 20°S, 84.5°W. (c),(d) Radar reflectivity for the corresponding times.

SEP is shown in Fig. 12. This schematic complements other conceptual models (e.g., Wood 2012, their Fig. 15; de Szoeke et al. 2012, their Fig. 17) and is meant to capture the most likely state of the boundary layer system over an ensemble of days.

To account for the east–west gradient in sea surface temperature, boundary layer depth, aerosol concentrations, and cloud liquid water path, we divided our results into regions east and west of 80°W. While there is some synoptic and year-to-year variation, in general the boundary layer in the western portion of the VOCALS-REx domain is typically warmer and deeper with fewer aerosols than the region closer to the South American coast (de Szoeke et al. 2012). The net result of these

features is a cloud deck with higher bases and tops in the west, but with a cloud thickness only slightly deeper in the west compared to the eastern portion of the domain (Fig. 7b; de Szoeke et al. 2012, their Fig. 5a). The observed difference between cloud-base and LCL heights, a proxy for the degree of turbulent mixing, was larger in the west compared to the east (de Szoeke et al. 2012). The weaker connection between the moist surface layer and the cloud deck, particularly during the daytime hours, resulted in thinner clouds, a more broken cloud field, and an increase in the mean and variability of shortwave radiation reaching the surface. Total drizzle area and conditional rain rates were both higher in the western region.

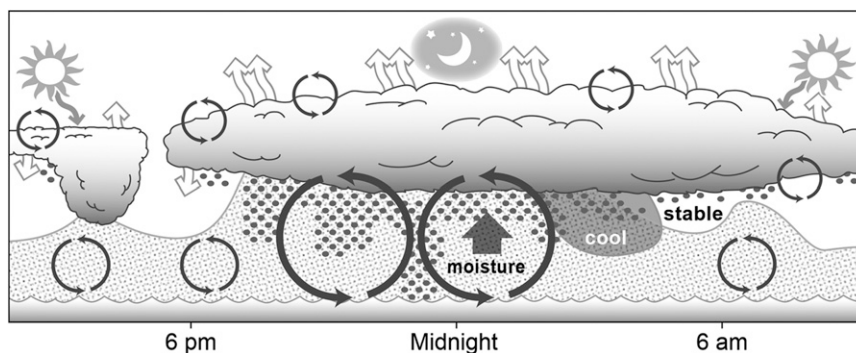


FIG. 12. Conceptual model showing the most common states of the stratocumulus cloud deck over the diurnal cycle. Precipitation (solid circles), surface-mixed-layer depth (shaded and dotted region), and turbulent mixing (circulating arrows) all vary regularly across the day.

Our study is consistent with work that shows the diurnal variation in marine stratocumulus clouds was largely driven by variations in subcloud turbulent moisture transport, which is strongly conditioned on vertical radiative flux divergence at cloud top (e.g., Nicholls 1984; Turton and Nicholls 1987). Vertical profiles of vertical velocity variance and potential temperature and moisture show that the subcloud boundary layer is well mixed at night and that the strength of turbulent mixing decreases strongly after sunrise. There is a cooling in subcloud potential temperatures after sunrise and vertical gradients in the subcloud potential temperature profiles increase, indicating an emerging stratification in the subcloud layer. This deep cooling observed in the subcloud layer is consistent with a recent modeling study over the VOCALS-REx domain (Tonizzzo et al. 2013), but it occurs somewhat later than the cooling generated in earlier simulations (e.g., Garreaud and Muñoz 2004, their Fig. 3e). In the late afternoon, when the boundary layer is most stably stratified, the potential temperature is on average 1 K warmer at cloud base than at the ocean surface.

Vertical profiles of water vapor mixing ratio show that these stable layers are very effective at trapping moisture near the surface (Fig. 3). During the day, the cloud is subject to solar heating, evaporation, and drying via entrainment of free-tropospheric air with little access to the surface moisture source. The ship-based data show significant cloud thinning and a marked reduction in precipitation during the late morning and into the afternoon. On average, a more decoupled state persists until after sunset, when net cloud-top radiative cooling creates negative buoyancy. Overnight, the descent of the negatively buoyant plumes is a source of turbulent kinetic energy and results in higher vertical velocity variance. The turbulence mixes all the way through the subcloud boundary layer and allows the cloud to tap the

reservoir of moisture at the surface, resulting in a more evenly distributed water vapor profile.

A new and interesting result came from the observations from the scanning C-band radar aboard the *RHB*, which showed that drizzle peaked overnight in the west and around sunrise in the east. Drizzle was reduced but still present throughout the day. The distribution of drizzle cell areas shows that drizzle is most likely to be organized into small discrete cells, with the most frequent drizzle cell area being less than 1 km^2 . In the western portion of the VOCALS-REx domain, where areal-averaged rain rates are higher, the number of drizzle cells and total drizzle area peak 2–3 h before sunrise, coincident with the diurnal peak in cloud-top height in the west. This observation implies that vertical mixing in the boundary layer may be reduced even before shortwave heating stabilizes the system. A possible mechanism to account for the reduction of precipitation after 0300 LST is that the higher peak areal density of drizzle cells in the west creates a large number of localized areas of subcloud evaporation that together are sufficient to reduce the vertical moisture flux in the early morning hours, making drizzle a self-limiting process. In the future, we hope to use HRDL data collected aboard the *RHB* to track the diurnal evolution of the surface mixed layer and look for gradients in backscatter that could be indicative of stable subcloud layers associated with heavy drizzle. The timing and rate of drizzle-induced stabilization of the boundary layer has important implications for the simulation of stratocumulus. For example, Boutle and Abel (2012) showed that the unrealistic moistening and cooling of the subcloud layer due to excessive drizzle production in the Met Office model was responsible for persistent decoupled bias overnight.

With the exception of near-surface aerosol concentrations, near-surface wind speeds, and conditional rain

TABLE A1. C-band radar scan strategy parameters during VOCALS-REx. Radar reflectivity, Doppler velocity, and spectral width variables were obtained in alternating PPI and RHI scans that repeated every 3 min.

	PRF (s ⁻¹)	Scan rate (° s ⁻¹)	Range resolution (m)	Max range (km)	PPI elevation angles (°)	RHI azimuth angles (°)	Scan duration (s)
PPI volume scan	2000	20	125	60	1, 2, 3, 4, 5, 6	—	120
RHI scan	2000	8	125	69	—	35, 125, 215, 305	40

rates, every variable examined in this study displayed a strong and persistent diurnal cycle. The magnitude of these daily variations is at least as large as the well-documented east–west gradient in stratocumulus properties. Diurnal variation in most parameters of this complex system can be directly linked to the presence or absence of deep boundary layer turbulent mixing. The observations collected aboard the *RHB* generally agree with data collected from other observational platforms during VOCALS-REx. Data from the ship provide a valuable tool for validating future modeling efforts of the diurnal cycle. These observations of the diurnal cycle can be used to test whether parameterizations of mixing and clouds are capable of simulating decoupled boundary layers.

Acknowledgments. The authors benefited greatly from numerous fruitful conversations with David Mechem during the development and refinement of this analysis. The surface aerosol concentration data were provided by the NOAA Pacific Marine Environmental Laboratory (PMEL) Atmospheric Chemistry Group. The liquid water path data are from Paquita Zuidema and Peter Minnett of the University of Miami. We are grateful to the crew and scientists of the NOAA ship *Ronald H. Brown* for their assistance in collecting this high-quality dataset. This work was funded by NOAA Grants GC08-252b and GC09-507, DOE Grant ASR DE-SC0006994, and NSF Grant ATM-0908420, with additional support for the lead author provided by NASA Earth and Space Science Fellowship NNX10AP43H. Any opinions, findings, and conclusions or recommendations expressed in this material are those of the author(s) and do not necessarily reflect the views of the National Science Foundation.

APPENDIX

Radar Calibration, Scan Strategy, and Z – R Relationship

The *RHB* C-band radar scan strategy for VOCALS-REx was built on experience using the same radar during the East Pacific Investigation of Climate Stratocumulus (EPIC Sc; Comstock et al. 2004) field campaign. The precipitation studied was characterized by

echo-top heights below 2 km, radar-echo depth between 500 and 2000 m, and precipitation cell areas from less than 1 km² to tens of square kilometers. The *RHB* radar has a 5.36-cm wavelength and a 0.95° beamwidth (Ryan et al. 2002). The antenna is mounted 33 m above the water line. Aging hardware limited the maximum scan rate to 20° s⁻¹. The scan strategy consisted of a plan position indicator (PPI) volume scan out to a 60-km range and a set of four range–height indicator (RHI) scans repeated every 3 min. Details of the scan strategy are provided in Table A1.

Ship motion correction was necessary to maintain the requested antenna-pointing angle relative to the horizon. The Seapath inertial navigation unit provided information on ship motion to the antenna controller and allowed for better than 0.4°-elevation-angle accuracy. The information from the inertial navigation system was also used to remove ship motion from the radial Doppler velocity data. The PPI reflectivity data were interpolated over a 250 m × 250 m × 500 m Cartesian grid, and the vertical layers from 0 to 500 and from 500 to 1000 m were retained for rain-rate (R) calculations. Rain rates presented in this paper are calculated from the composited maximum values of the two layers for each horizontal grid cell. This represents our best estimate of cloud-base rain rate. We make no attempt to account for subcloud evaporation of the estimated cloud-base rain rates. To quantify rain-rate errors resulting from systematic biases in reflectivity Z , rain rates were also derived with a ±2-dBZ calibration error (Comstock et al. 2004). Sea clutter was frequently present in the radar domain near the ship. As part of quality control, all data within a 25-km range from the ship were removed from the rain maps and not used in the calculation of areal-average rain rates.

A key consideration for the rain-rate estimates was the choice of Z – R relationship. We use a simple adaptation of the EPIC Sc (Comstock et al. 2004) C-band radar Z – R relationship that accounts for the more frequent high reflectivities ($Z > 30$ dBZ) observed during VOCALS-REx. Reflectivities greater than 45 dBZ were observed by the C-band radar in VOCALS-REx but were not sampled in situ by either ship or aircraft sensors. The associated drop size distribution and Z – R relationship for such regions of comparatively intense precipitation are unknown. We dealt with reflectivities

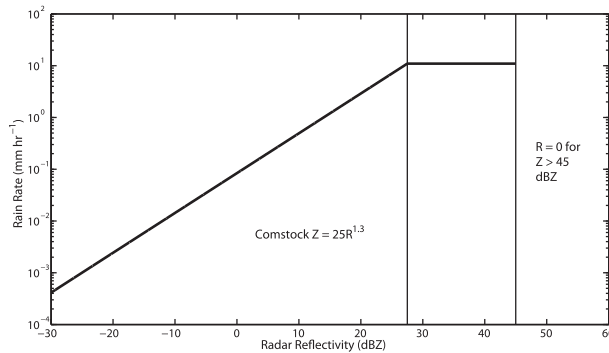


FIG. A1. The Z - R function used to calculate rain rates for the VOCALS rain map data product.

greater than 30 dBZ by applying an upper threshold to the EPIC C-band radar drizzle Z - R relationship developed by Comstock et al. (2004). The resulting piecewise Z - R relationship is shown in Fig. A1. Pixels with Z values less than or equal to 27.5 dBZ were converted to rain rates using Comstock et al.'s $Z = 25R^{1.3}$ (where R is in mm h^{-1} and Z is in $\text{mm}^6 \text{m}^{-3}$). Values between 27.5 and 45 dBZ were set to $R = 11 \text{ mm h}^{-1}$, which equals the Comstock et al. value for $Z = 27.5 \text{ dBZ}$. Over the whole dataset, less than 0.001% of all of the rainy pixels had $Z > 45 \text{ dBZ}$. To avoid substantial overestimation of mean rain rates, these outliers were disregarded for the computation of areal-average and conditional-average rain rates. The areal-average rates for the final Z - R relationship are in reasonable agreement with previous estimates from EPIC Sc (Comstock et al. 2004) and *CloudSat* (Leon et al. 2008), as well as with VOCALS-related modeling studies (Mechem et al. 2012). The piecewise Z - R relationship itself is monotonic and continuous up to 45 dBZ, and the resulting rain-rate artifact—located at 27.5 dBZ—is confined to the top bin of the distribution. In the absence of other information to constrain the Z - R relationship, this estimation method is advantageous because it is simple and transparent.

The *RHB* C-band radar data were used to produce 768 h of rain-rate histograms, areal-average rain rates (including zero values), and conditional-average rain rates (mm day^{-1}). Conditional-average rain rates are defined as the average rain rate for all rainy pixels (i.e., those pixels that exceeded a range-dependent sensitivity threshold). The time series of estimated cloud-base areal-average rain rate during the two legs of the VOCALS-REx cruise are shown in Fig. A2. The areal-average rain rates during leg 1 varied from 0 to 6 mm day^{-1} . Leg 2 had weaker drizzle, with a maximum of about 3 mm day^{-1} . If less than 100 km^2 (1600 pixels) of rainy pixels were detected on average for all scans

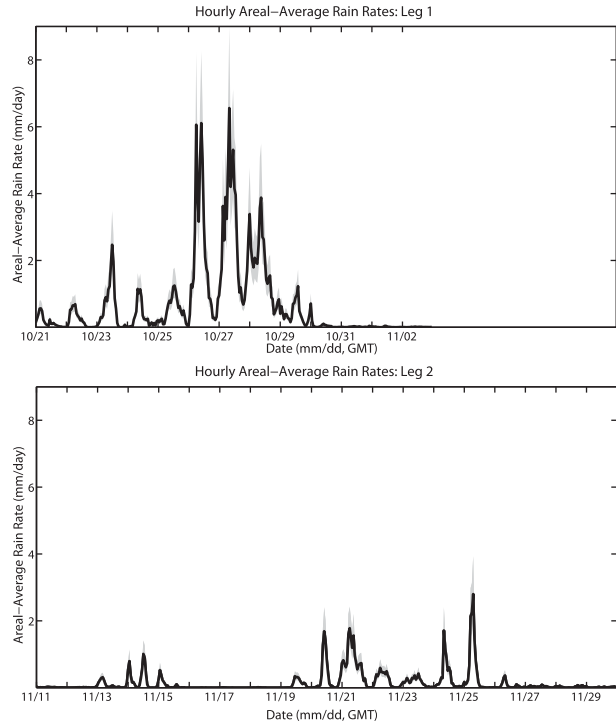


FIG. A2. Hourly averaged time series of cloud-base rain rate (black lines) from (top) leg 1 and (bottom) leg 2 of VOCALS-REx. The uncertainty in rainfall associated with a ± 2 -dBZ calibration error is shown with gray shading. The x axis is scaled so that the same horizontal distance represents 1 day of data in both plots.

over the course of an hour, then the hourly average conditional rain rate was stored as a missing value.

REFERENCES

- Abel, S. J., D. N. Walters, and G. Allen, 2010: Evaluation of stratocumulus cloud precipitation in the Met Office forecast model during VOCALS-REx. *Atmos. Chem. Phys. Discuss.*, **10**, 16 797–16 835, doi:10.5194/acpd-10-16797-2010.
- Allen, G., and Coauthors, 2011: South east Pacific atmospheric composition and variability sampled along 20°S during VOCALS-REx. *Atmos. Chem. Phys.*, **11**, 5237–5262, doi:10.5194/acp-11-5237-2011.
- Bennartz, R., 2007: Global assessment of marine boundary layer cloud droplet number concentration from satellite. *J. Geophys. Res.*, **112**, D02201, doi:10.1029/2006JD007547.
- Betts, A. K., 1990: Diurnal variation of California coastal stratocumulus from two days of boundary layer soundings. *Tellus*, **42A**, 302–304.
- Bony, S., and J.-L. Dufresne, 2005: Marine boundary layer clouds at the heart of tropical cloud feedback uncertainties in climate models. *Geophys. Res. Lett.*, **32**, L20806, doi:10.1029/2005GL023851.
- , and Coauthors, 2006: How well do we understand and evaluate climate change feedback processes? *J. Climate*, **19**, 3445–3482.
- Boutle, I. A., and S. J. Abel, 2012: Microphysical controls on the stratocumulus topped boundary-layer structure during VOCALS-REx. *Atmos. Chem. Phys.*, **12**, 2849–2863, doi:10.5194/acp-12-2849-2012.

- Bretherton, C. S., and M. C. Wyant, 1997: Moisture transport, lower-tropospheric stability, and decoupling of cloud-topped boundary layers. *J. Atmos. Sci.*, **54**, 148–167.
- , and Coauthors, 2004: The EPIC 2001 stratocumulus study. *Bull. Amer. Meteor. Soc.*, **85**, 976–977.
- , R. Wood, R. C. George, D. Leon, G. Allen, and X. Zheng, 2010: Southeast Pacific stratocumulus clouds, precipitation and boundary layer structure sampled along 20°S during VOCALS-REx. *Atmos. Chem. Phys.*, **10**, 10639–10654, doi:10.5194/acp-10-10639-2010.
- Comstock, K. K., R. Wood, S. E. Yuter, and C. S. Bretherton, 2004: Reflectivity and rain rate in and below drizzling stratocumulus. *Quart. J. Roy. Meteor. Soc.*, **130**, 2891–2918.
- , C. S. Bretherton, and S. E. Yuter, 2005: Mesoscale variability and drizzle in southeast Pacific stratocumulus. *J. Atmos. Sci.*, **62**, 3792–3807.
- , S. E. Yuter, R. Wood, and C. S. Bretherton, 2007: The three-dimensional structure and kinematics of drizzling stratocumulus. *Mon. Wea. Rev.*, **135**, 3767–3784.
- de Szoeke, S. P., C. W. Fairall, D. E. Wolfe, L. Bariteau, and P. Zuidema, 2010: Surface flux observations on the southeastern tropical Pacific Ocean and attribution of SST errors in coupled ocean–atmosphere models. *J. Climate*, **23**, 4152–4174.
- , S. E. Yuter, D. Mechem, C. W. Fairall, C. D. Burleyson, and P. Zuidema, 2012: Observations of stratocumulus and their effect on the eastern Pacific surface heat budget along 20°S. *J. Climate*, **25**, 8542–8567.
- Duynkerke, P. G., 1989: The diurnal variation of a marine stratocumulus cloud: A model sensitivity study. *Mon. Wea. Rev.*, **117**, 1710–1725.
- Feingold, G., I. Koren, H. Wang, H. Xue, and W. A. Brewer, 2010: Precipitation-generated oscillations in open cellular cloud fields. *Nature*, **466**, 849–852, doi:10.1038/nature09314.
- Garreaud, R. D., and R. C. Muñoz, 2004: The diurnal cycle in circulation and cloudiness over the subtropical southeast Pacific: A modeling study. *J. Climate*, **17**, 1699–1710.
- George, R. C., and R. Wood, 2010: Subseasonal variability of low cloud radiative properties over the southeast Pacific. *Atmos. Chem. Phys.*, **10**, 4047–4063, doi:10.5194/acp-10-4047-2010.
- Grund, C. J., R. M. Banta, J. L. George, J. N. Howell, M. J. Post, R. A. Richter, and A. M. Weickmann, 2001: High-resolution Doppler lidar for boundary layer and cloud research. *J. Atmos. Oceanic Technol.*, **18**, 376–393.
- Hartmann, D. L., M. E. Ockert-Bell, and M. L. Michelson, 1992: The effect of cloud type on Earth's energy balance: Global analysis. *J. Climate*, **5**, 1281–1304.
- Jaeglé, L., P. K. Quinn, T. S. Bates, B. Alexander, and J.-T. Lin, 2011: Global distribution of sea salt aerosols: New constraints from in situ and remote sensing observations. *Atmos. Chem. Phys.*, **11**, 3137–3157, doi:10.5194/acp-11-3137-2011.
- James, D. G., 1959: Observations from aircraft of temperatures and humidities near stratocumulus clouds. *Quart. J. Roy. Meteor. Soc.*, **85**, 120–130.
- Jones, C. R., C. S. Bretherton, and D. Leon, 2011: Coupled vs. decoupled boundary layers in VOCALS-REx. *Atmos. Chem. Phys.*, **11**, 7143–7153, doi:10.5194/acp-11-7143-2011.
- Klein, S. A., and D. L. Hartmann, 1993: The seasonal cycle of low stratiform clouds. *J. Climate*, **6**, 1587–1606.
- Leon, D. C., Z. Wang, and D. Liu, 2008: Climatology of drizzle in marine boundary layer clouds based on 1 year of data from CloudSat and Cloud-Aerosol Lidar and Infrared Pathfinder Satellite Observations (CALIPSO). *J. Geophys. Res.*, **113**, D00A14, doi:10.1029/2008JD009835.
- Lewellen, D. C., and W. S. Lewellen, 1998: Large-eddy boundary layer entrainment. *J. Atmos. Sci.*, **55**, 2645–2665.
- Mechem, D. B., S. E. Yuter, and S. P. de Szoeke, 2012: Thermodynamic and aerosol controls in southeast Pacific stratocumulus. *J. Atmos. Sci.*, **69**, 1250–1266.
- Medeiros, B., D. L. Williamson, C. Hannay, and J. G. Olson, 2012: Southeast Pacific stratocumulus in the Community Atmosphere Model. *J. Climate*, **25**, 6175–6192.
- Moeng, C.-H., S. Shen, and D. A. Randall, 1992: Physical processes within the nocturnal stratus-topped boundary layer. *J. Atmos. Sci.*, **49**, 2384–2401.
- Moran, K. P., S. Pezoa, C. Fairall, C. Williams, T. Ayers, Al. Brewer, S. P. de Szoeke, and V. Ghate, 2011: A motion-stabilized W-band radar for shipboard cloud observations and airborne studies of sea spray. *Bound.-Layer Meteor.*, **143**, 3–24.
- Nicholls, S., 1984: The dynamics of stratocumulus: Aircraft observations and comparisons with a mixed layer model. *Quart. J. Roy. Meteor. Soc.*, **110**, 783–820.
- Painemal, D., R. Garreaud, J. Rutllant, and P. Zuidema, 2010: Southeast Pacific stratocumulus: High-frequency variability and mesoscale structures over San Felix Island. *J. Appl. Meteor. Climatol.*, **49**, 463–477.
- , P. Minnis, and L. O'Neill, 2013: The diurnal cycle of cloud-top height and cloud cover over the southeast Pacific as observed by GOES-10. *J. Atmos. Sci.*, **70**, 2393–2408.
- Rahn, D. A., and R. D. Garreaud, 2010: Marine boundary layer over the subtropical southeast Pacific during VOCALS-REx—Part 1: Mean structure and diurnal cycle. *Atmos. Chem. Phys.*, **10**, 4491–4506, doi:10.5194/acp-10-4491-2010.
- Rogers, D. P., X. Yang, P. M. Norris, D. W. Johnson, G. M. Martin, C. A. Friehe, and B. W. Berger, 1995: Diurnal evolution of the cloud-topped marine boundary layer. Part I: Nocturnal stratocumulus development. *J. Atmos. Sci.*, **52**, 2953–2966.
- Ryan, M., M. J. Post, B. Martner, J. Novak, and L. Davis, 2002: The NOAA Ron Brown's shipboard Doppler precipitation radar. Preprints, *Sixth Symp. on Integrated Observing Systems*, Orlando, FL, Amer. Meteor. Soc., P1.7. [Available online at https://ams.confex.com/ams/annual2002/techprogram/paper_27707.htm.]
- Shank, L. M., and Coauthors, 2012: Organic matter and non-refractory aerosol over the remote southeast Pacific: Oceanic and combustion sources. *Atmos. Chem. Phys.*, **12**, 557–576, doi:10.5194/acp-12-557-2012.
- Taleb, N. N., 2007: *The Black Swan: The Impact of the Highly Improbable*. Random House, 366 pp.
- Tang, I. N., 1996: Chemical and size effects on hygroscopic aerosols on light scattering coefficients. *J. Geophys. Res.*, **101** (D14), 19245–19250.
- Terai, C., 2011: Drizzle and the aerosol indirect effect in marine stratocumulus. M.S. thesis, Department of Atmospheric Sciences, University of Washington, 91 pp.
- Tomlinson, J. M., R. Li, and D. R. Collins, 2007: Physical and chemical properties of the aerosol within the southeastern Pacific marine boundary layer. *J. Geophys. Res.*, **112**, D12211, doi:10.1029/2006JD007771.
- Toniazzo, T., S. J. Abel, R. Wood, C. R. Mechoso, G. Allen, and L. C. Shaffrey, 2011: Large-scale and synoptic meteorology in the south-east Pacific during the observations campaign VOCALS-REx in austral Spring 2008. *Atmos. Chem. Phys.*, **11**, 4977–5009, doi:10.5194/acp-11-4977-2011.

- , F. Sun, C. R. Mechoso, and A. Hall, 2013: A regional modeling study of the diurnal cycle in the lower troposphere in the south-eastern tropical Pacific. *Climate Dyn.*, **41**, 1899–1922, doi:10.1007/s00382-012-1598-3.
- Turton, J. D., and S. Nicholls, 1987: A study of the diurnal variation of stratocumulus using a mixed layer model. *Quart. J. Roy. Meteor. Soc.*, **113**, 969–1009.
- vanZanten, M. C., and B. Stevens, 2005: Observations of the structure of heavily precipitating marine stratocumulus. *J. Atmos. Sci.*, **62**, 4327–4342.
- Wang, H., and G. Feingold, 2009: Modeling mesoscale cellular structures and drizzle in marine stratocumulus. Part I: Impact of drizzle on the formation and evolution of open cells. *J. Atmos. Sci.*, **66**, 3237–3256.
- Wang, S., and Q. Wang, 1994: Roles of drizzle in a one-dimensional third-order turbulence closure model of the nocturnal stratocumulus marine boundary layer. *J. Atmos. Sci.*, **51**, 1559–1576.
- Weare, B., 1996: Evaluation of the vertical structure of zonally averaged cloudiness and its variability in the Atmospheric Model Intercomparison Project. *J. Climate*, **9**, 3419–3431.
- Wood, R., 2012: Stratocumulus clouds. *Mon. Wea. Rev.*, **140**, 2373–2423.
- , and C. S. Bretherton, 2004: Boundary layer depth, entrainment, and decoupling in the cloud-capped subtropical and tropical marine boundary layer. *J. Climate*, **17**, 3576–3588.
- , K. K. Comstock, C. S. Bretherton, C. Cornish, J. Tomlinson, D. R. Collins, and C. W. Fairall, 2008: Open cellular structure in marine stratocumulus sheets. *J. Geophys. Res.*, **113**, D12207, doi:10.1029/2007JD009371.
- , M. Köhler, R. Bennartz, and C. O'Dell, 2009: The diurnal cycle of surface divergence over the global oceans. *Quart. J. Roy. Meteor. Soc.*, **135**, 1484–1493.
- , and Coauthors, 2011: The VAMOS Ocean-Cloud-Atmosphere-Land Study Regional Experiment (VOCALS-REx): Goals, platforms, and field operations. *Atmos. Chem. Phys.*, **11**, 627–654, doi:10.5194/acp-11-627-2011.
- Wyant, M. C., C. S. Bretherton, J. T. Bacmeister, J. T. Kiehl, I. M. Held, M. Zhao, S. A. Klein, and B. J. Soden, 2006: A comparison of low-latitude cloud properties and their response to climate change in three AGCMs sorted into regimes using mid-tropospheric vertical velocity. *Climate Dyn.*, **27**, 261–279, doi:10.1007/s00382-006-0138-4.
- , and Coauthors, 2010: The PreVOCA experiment: Modeling the lower troposphere in the southeast Pacific. *Atmos. Chem. Phys.*, **10**, 4757–4774, doi:10.5194/acp-10-4757-2010.
- Yang, M., and Coauthors, 2011: Atmospheric sulfur cycling in the southeastern Pacific—Longitudinal distribution, vertical profile, and diel variability observed during VOCALS-REx. *Atmos. Chem. Phys.*, **11**, 5079–5097, doi:10.5194/acp-11-5079-2011.
- Zuidema, P., E. R. Westwater, C. Fairall, and D. Hazen, 2005: Ship-based liquid water path estimates in marine stratocumulus. *J. Geophys. Res.*, **110**, D20206, doi:10.1029/2005JD005833.
- , D. Painemal, S. de Szoeker, and C. Fairall, 2009: Stratocumulus cloud-top height estimates and their climatic implications. *J. Climate*, **22**, 4652–4666.
- , D. Leon, A. Pazmany, and M. Cadetdu, 2012: Aircraft millimeter-wave passive sensing of cloud liquid water and water vapor during VOCALS-REx. *Atmos. Chem. Phys.*, **12**, 355–369, doi:10.5194/acp-12-355-2012.